25. N. H. Schlieben *et al.*, *J. Mol. Biol.* **349**, 801–813 (2005).
26. K. Tauber *et al.*, *Chemistry* **19**, 4030–4035 (2013).
27. See supplementary materials on *Science* Online.
28. A. C. Price, Y.-M. Zhang, C. O. Rock, S. W. White, *Structure* **12**, 417–428 (2004).
29. The Ph-AmDH tolerates different buffers well (i.e., ammonium chloride, formate, borate, citrate, acetate, oxalate). However, the homotetrameric LBv-ADHs contains two Mg^{2+} centers; therefore, strong chelators such as oxalate, citrate, and acetate must be avoided as buffer salts. Removal of these Mg^{2+} ions inactivates the enzyme (*32*).
30. B. R. Bommarius, M. Schürmann, A. S. Bommarius, *Chem. Commun.* **50**, 14953–14955 (2014).
31. R. Cannio, M. Rossi, S. Bartolucci, *Eur. J. Biochem.* **222**, 345–352 (1994).
32. K. Niefind, J. Müller, B. Riebel, W. Hummel, D. Schomburg, *J. Mol. Biol.* **327**, 317–328 (2003).

ACKNOWLEDGMENTS

The research leading to these results received funding from the European Union's Seventh Framework Programme FP7/2007-2013 under grant agreement 266025 (BIONEXGEN). The project leading to this application has received funding from the European Research Council under the European Union's Horizon 2020 research and innovation program (grant agreement no. 638271, BioSusAmin). T.K. and N.S.S. received funding from UK Biotechnology and Biological Sciences Research Council (BBSRC; BB/K0017802/1). N.J.T. is grateful to the Royal Society for a Wolfson Research Merit Award. Some aspects of the results reported here are the subject of a provisional patent application. Author contributions: F.G.M. and N.J.T. conceived the project and wrote the manuscript; F.G.M. planned the experiments, expressed and purified the AmDHs, performed the biocatalytic reactions, and analyzed the data; T.K. performed the gene cloning of all AmDHs and purified the ADHs; N.S.S. and M.B. provided intellectual and technical support; and M.B. and BASF provided the ADHs. We thank R. Heath for a preliminary kinetic assay of the Ph-AmDH.

SUPPLEMENTARY MATERIALS

www.sciencemag.org/content/349/6255/1525/suppl/DC1
Materials and Methods
Figs. S1 to S12
Tables S1 to S20
References (*33*–*36*)

30 June 2015; accepted 14 August 2015
10.1126/science.aac9283

BATTERIES

Alkaline quinone flow battery

Kaixiang Lin,[1] Qing Chen,[2] Michael R. Gerhardt,[2] Liuchuan Tong,[1] Sang Bok Kim,[1] Louise Eisenach,[3] Alvaro W. Valle,[3] David Hardee,[1] Roy G. Gordon,[1,2]* Michael J. Aziz,[2]* Michael P. Marshak[1,2]*

Storage of photovoltaic and wind electricity in batteries could solve the mismatch problem between the intermittent supply of these renewable resources and variable demand. Flow batteries permit more economical long-duration discharge than solid-electrode batteries by using liquid electrolytes stored outside of the battery. We report an alkaline flow battery based on redox-active organic molecules that are composed entirely of Earth-abundant elements and are nontoxic, nonflammable, and safe for use in residential and commercial environments. The battery operates efficiently with high power density near room temperature. These results demonstrate the stability and performance of redox-active organic molecules in alkaline flow batteries, potentially enabling cost-effective stationary storage of renewable energy.

The cost of photovoltaic (PV) and wind electricity has dropped so much that one of the largest barriers to getting most of our electricity from these renewable sources is their intermittency (*1*–*3*). Batteries provide a means to store electrical energy; however, traditional, enclosed batteries maintain discharge at peak power for far too short a duration to adequately regulate wind or solar power output (*1*, *2*). In contrast, flow batteries can independently scale the power and energy components of the system by storing the electro-active species outside the battery container itself (*3*–*5*). In a flow battery, the power is generated in a device resembling a fuel cell, which contains electrodes separated by an ion-permeable membrane. Liquid solutions of redox-active species are pumped into the cell, where they can be charged and discharged, before being returned to storage in an external storage tank. Scaling the amount of energy to be stored thus involves simply making larger tanks (Fig. 1A). Existing flow batteries are based on metal ions in acidic solution, but challenges with corrosivity, hydrogen evolution, kinetics, materials cost and abundance, and efficiency thus far have prevented large-scale commercialization. The use of anthraquinones in an acidic aqueous flow battery can dramatically

[1]Department of Chemistry and Chemical Biology, Harvard University, 12 Oxford Street, Cambridge, MA 02138, USA. [2]Harvard John A. Paulson School of Engineering and Applied Sciences, 29 Oxford Street, Cambridge, MA 02138, USA. [3]Harvard College, Cambridge, MA 02138, USA.
*Corresponding author. E-mail: aziz@seas.harvard.edu (M.J.A.); gordon@chemistry.harvard.edu (R.G.G.); michael.marshak@colorado.edu (M.P.M.)

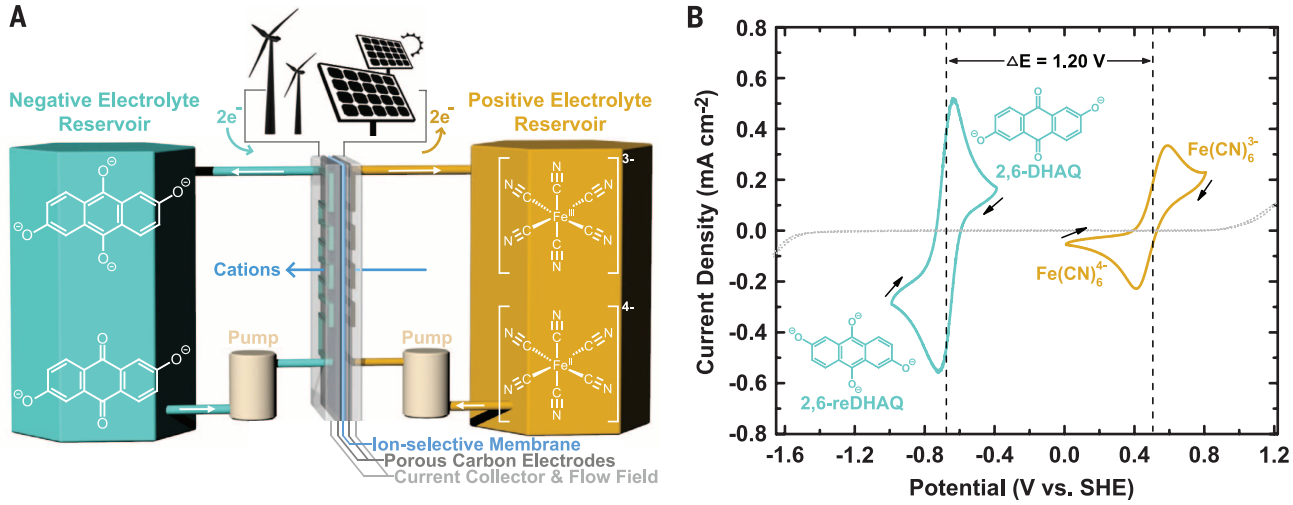

Fig. 1. Cyclic voltammetry of electrolyte and cell schematic. (**A**) Schematic of cell in charge mode. Cartoon on top of the cell represents sources of electrical energy from wind and solar. Curved arrows indicate direction of electron flow, and white arrows indicate electrolyte solution flow. Blue arrow indicates migration of cations across the membrane. Essential components of electrochemical cells are labeled with color-coded lines and text. The molecular structures of oxidized and reduced species are shown on corresponding reservoirs. (**B**) Cyclic voltammogram of 2 mM 2,6-DHAQ (dark cyan curve) and ferrocyanide (gold curve) scanned at 100 mV/s on glassy carbon electrode; arrows indicate scan direction. Dotted line represents CV of 1 M KOH background scanned at 100 mV/s on graphite foil electrode.

reduce battery costs (*6*, *7*); however, the use of bromine in the other half of the system precludes deployment in residential communities owing to toxicity concerns.

We demonstrate that quinone-based flow batteries can be adapted to alkaline solutions, where hydroxylated anthraquinones are highly soluble and bromine can be replaced with the nontoxic ferricyanide ion (*8*, *9*)—a food additive (*10*). Functionalization of 9,10-anthraquinone (AQ) with electron-donating groups such as OH has been shown to lower the reduction potential and expand the battery voltage (*6*). In alkaline solution, these OH groups are deprotonated to provide solubility and greater electron donation capability, which results in an increase in the open-circuit voltage (OCV) of 47% over the previously reported system. Because functionalization away from the ketone group provides molecules with the highest solubility (*11*, *12*), we initially targeted commercially available 2,6-dihydroxyanthraquinone (2,6-DHAQ), which we find exhibits a room-temperature solubility of >0.6 M in 1 M KOH. This system can achieve power densities of >0.45 W cm^{-2} at room temperature and 0.7 W cm^{-2} at 45°C.

The use of alkaline electrolyte exploits pH as a parameter to shift the thermodynamic potentials of proton-dependent reactions to more negative values. In acid solutions, AQ undergoes a two-electron two-proton reduction at a single potential, which shifts to more negative values as the pH increases (*6*). When the pH exceeds 12, the reduction potential of 2,6-DHAQ becomes pH-independent because the reduced species is generated in its fully deprotonated form (fig. S1). In contrast with the pH-dependent electrochemical behavior of quinones (negative terminal), the ferro/ferricyanide redox couple (positive terminal) has a pH-independent redox potential. This contrasting pH dependence can be exploited through the development of low–reduction potential quinones at high pH. The cyclic voltammograms (CVs) of 2,6-DHAQ and ferro/ferricyanide predict an equilibrium cell potential of 1.2 V upon combination of these two half-reactions (Fig. 1B). A quantitative analysis of the CV of 2,6-DHAQ at pH 14 (fig. S2) revealed redox behavior consistent with two one-electron reductions at potentials separated by only 0.06 V, with a rapid kinetic rate similar to that of quinones in acid (*6*). This behavior raises interesting questions about the relationship between quinone redox and hydrogen bonding (*13*).

Cell testing was performed at 20°C with solutions of 0.5 M 2,6-DHAQ dipotassium salt and 0.4 M $K_4Fe(CN)_6$, both dissolved in 1 M KOH. These solutions were pumped through a flow cell constructed from graphite flow plates and carbon paper electrodes, which were separated by a Nafion membrane. A charging current of 0.1 A cm^{-2} was applied to charge the cell, and polarization curves were measured at 10, 50, and 100% states of quinone charge (SOC). The OCV is 1.2 V at 50%

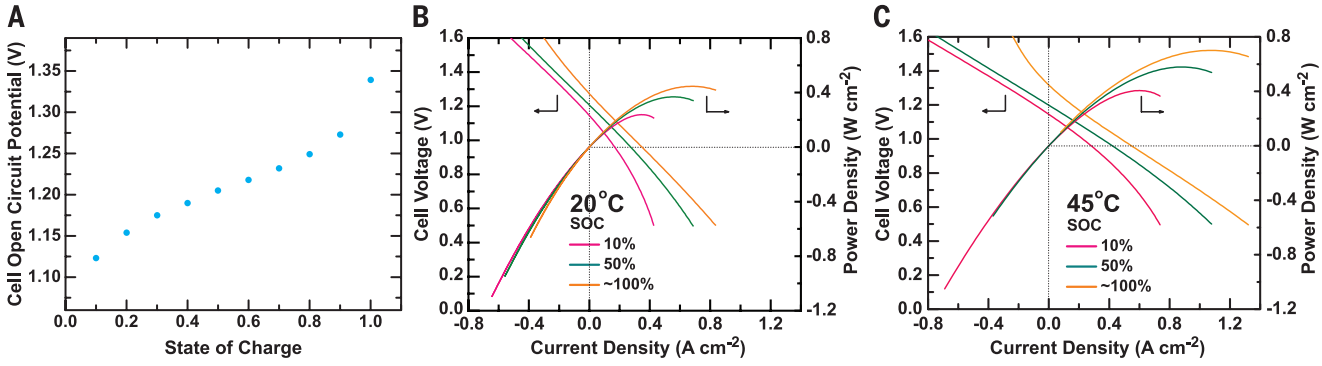

Fig. 2. Cell performance. (**A**) Cell open-circuit voltage versus state of charge. All potentials were taken when cell voltage stabilized to within ±1 mV. One hundred percent SOC was reached by potentiostatic holding at 1.5 V until the current decreased to below 20 mA/cm^2. (**B** and **C**) Cell voltage and power density versus current density at 20° and 45°C, respectively, at 10, 50, and ~100% SOC. Electrolyte composition: At 20°C, 0.5 M 2,6-DHAQ and 0.4 M ferrocyanide were used in negative electrolyte and positive electrolyte, respectively. At 45°C, both concentrations were doubled. In both cases, potassium hydroxide content started at 1 M for both sides in the fully discharged state.

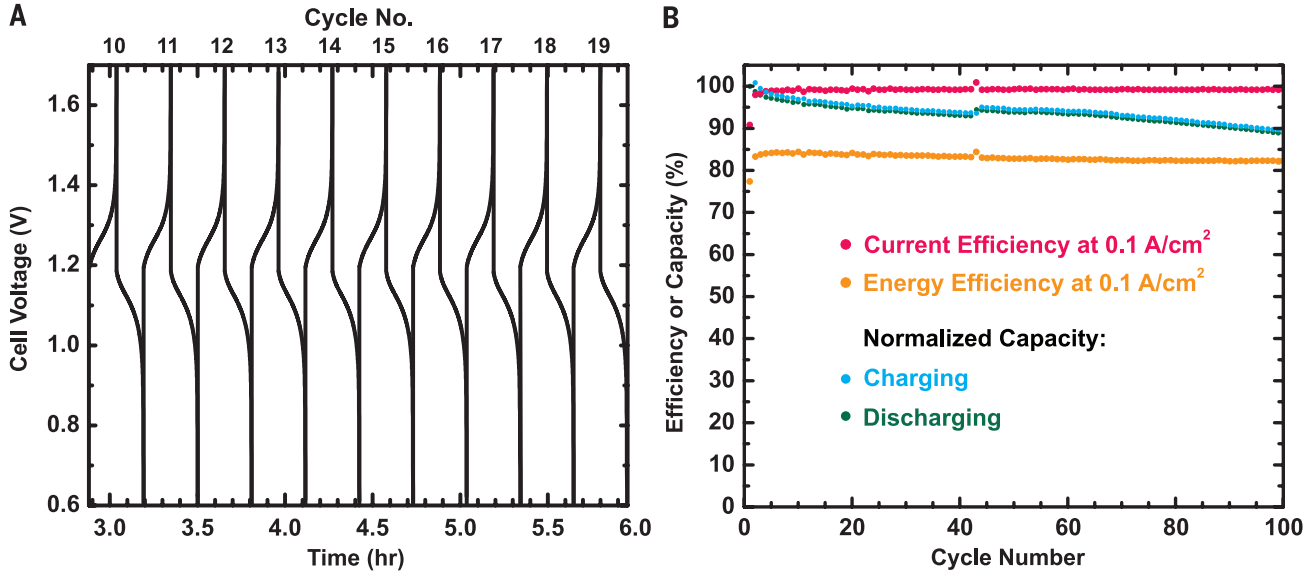

Fig. 3. Cell cycling performance. (**A**) Representative voltage versus time curves during 100 charge-discharge cycles at 0.1 A/cm^2, recorded between the 10th and 19th cycles. (**B**) Capacity retention, current efficiency, and energy efficiency values of 100 cycles. Normalized capacity is evaluated based on the capacity of the first charge and discharge cycle.

SOC; its dependence on SOC is shown in Fig. 2A. The polarization curves (Fig. 2B) show no sign of redox kinetic limitations and exhibit a peak galvanic power density exceeding 0.4 W cm^{-2}.

The cell was cycled at a constant current density of ±0.1 A cm^{-2} for 100 cycles (Fig. 3A). The current efficiency exceeded 99%, with a stable round-trip energy efficiency of 84%. A 0.1% loss in capacity per cycle was observed during cycling, which appears to be a continuous loss of electrolyte over the 100 cycles. Three possible loss mechanisms were explored: chemical decomposition, electrolyte crossover through the membrane, and leakage from the pumping system. Chemical and electrochemical stability studies showed that the negative electrolyte is stable. Ten millimolar 2,6-DHAQ was heated in 5 M KOH solution at 100°C for 30 days and was characterized by proton nuclear magnetic resonance (NMR). Cycled negative electrolyte was also collected and characterized by the same method; both studies showed no degradation product at the sensitivity level of 1% (fig. S3). Membrane crossover contamination has been a common challenge in acid-based redox flow batteries, where most electro-active molecules are either neutral or positive and tend to migrate through proton-conductive membranes (*5*). In this alkaline system, however, all the electro-active molecules remain negatively charged in all charge states, leading to a dramatic decrease in the degree of crossover during cell cycling. Cyclic voltammetry of the ferro/ferricyanide electrolyte collected at the end of cycling showed no evidence of the presence of 2,6-DHAQ. This observation places an upper limit on crossover of 0.8% of the DHAQ, implying a crossover current density of <2.5 μA cm^{-2} (fig. S4). Finally, hydraulic leakage was investigated because an apparent but unquantifiable small decrease in fluid levels was observed in the reservoirs. After cell cycling, the cell was washed with deionized water until no coloration of eluent could be observed. The cell was then disassembled; coloration was found on the gaskets, indicating the likely site of electrolyte leakage (fig. S5). This source of capacity loss—equivalent to roughly eight drops in our system—is expected to become negligible as system size is scaled up.

By increasing the temperature to 45°C, the peak galvanic power density increases from 0.45 to ~0.7 W cm^{-2} (Fig. 2C), as the cell area-specific resistance (ASR) decreases from about 0.878 to 0.560 ohm cm^2, estimated from the linear parts of the polarization curves in Fig. 2. Most of this ASR decrease comes from a change in the high-frequency ASR (r_{hf}) measured by electrochemical impedance spectroscopy (fig. S6). In both cases, the r_{hf} contributes more than 70% of the ASR and is indeed the limiting factor to the cell current and power outputs. The r_{hf} is dominated by the resistance of the membrane, which is an order of magnitude higher than the resistance of the same membrane in a pH 0 acid solution (*14*).

The sluggish kinetics of the hydrogen evolution reaction in alkaline solution on carbon electrodes results in a larger practical stability window in base rather than in acid (fig. S7). Consequently, quinones with substantially more negative reduction potentials are feasible as negative electrolyte materials. Preliminary investigations into the synthesis of different hydroxy-substituted anthraquinones suggest that further increases in cell potential are possible. Self-condensation reactions of substituted benzene yield 2,3,6,7-tetrahydroxyAQ (THAQ) (*15*) and 1,5-dimethyl-2,6-DHAQ (15-DMAQ) (figs. S8 and S9). The CVs of these species in 1 M KOH suggest cell potentials versus ferri/ferrocyanide approaching 1.35 V (Fig. 4, A and B), which exceeds that of many aqueous rechargeable batteries (Fig. 4C).

The cyanide ions in both ferro- and ferricyanide are bound too tightly to be released under most conditions. Consequently, it is nontoxic in both oxidized and reduced forms and is even

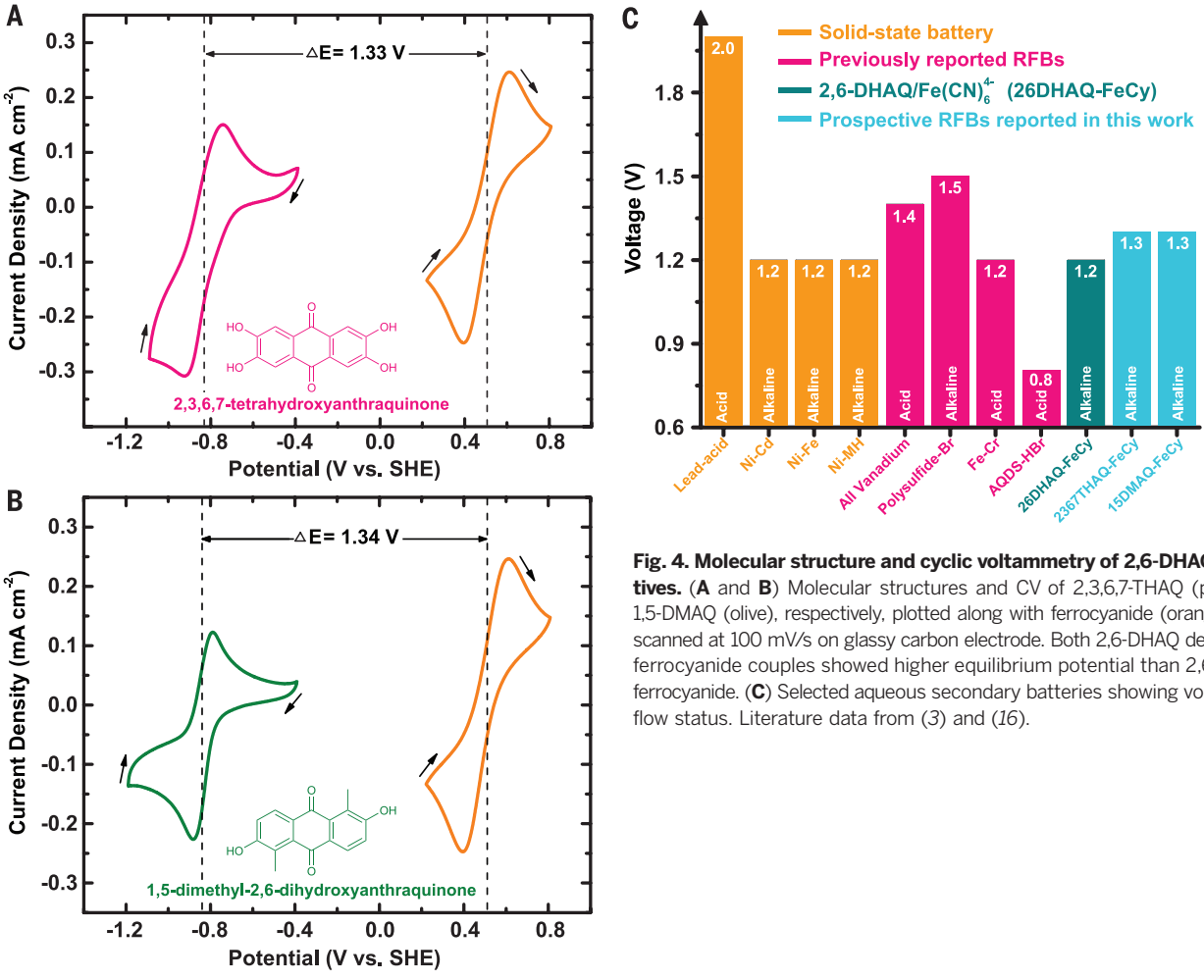

Fig. 4. Molecular structure and cyclic voltammetry of 2,6-DHAQ derivatives. (**A** and **B**) Molecular structures and CV of 2,3,6,7-THAQ (pink) and 1,5-DMAQ (olive), respectively, plotted along with ferrocyanide (orange curve) scanned at 100 mV/s on glassy carbon electrode. Both 2,6-DHAQ derivatives/ferrocyanide couples showed higher equilibrium potential than 2,6-DHAQ/ferrocyanide. (**C**) Selected aqueous secondary batteries showing voltage and flow status. Literature data from (*3*) and (*16*).

permitted for use as a food additive (*10*). The use of ferrocyanide offers notable advantages over bromine because it is nonvolatile and noncorrosive, allowing simpler and less expensive materials of construction. In addition, these tri- and tetra-anionic organometallic molecules exhibit low crossover rates through cation-exchange membranes.

The results reported herein highlight the ability of hydroxy-substituted anthraquinone and ferrocyanide to function as stable flow battery electrolytes in alkaline solution. The use of organic and organometallic coordination complexes in base, rather than aqueous metal ions in acid, resolves serious cost, corrosion, and safety concerns of previous flow battery chemistries. Alkaline flow batteries can compensate for higher membrane resistance with higher voltage, leading to performance similar to that of their acidic counterparts. In addition, quinone-ferrocyanide alkaline chemistry avoids the membrane crossover, corrosivity, toxicity, and regulations associated with bromine. This reduced corrosivity can lead to a substantially lower materials cost because many components can be made of inexpensive polyolefin or poly(vinyl chloride) plastics.

REFERENCES AND NOTES

1. B. Dunn, H. Kamath, J.-M. Tarascon, *Science* **334**, 928–935 (2011).
2. Z. Yang *et al*., *Chem. Rev.* **111**, 3577–3613 (2011).
3. T. Nguyen, R. F. Savinell, *Electrochem. Soc. Interface* **19**, 54–56 (2010).
4. D. Biello, *Sci. Am.* **311**, 66–71 (November 2014).
5. M. Skyllas-Kazacos, M. H. Chakrabarti, S. A. Hajimolana, F. S. Mjalli, M. Saleem, *J. Electrochem. Soc.* **158**, R55–R79 (2011).
6. B. Huskinson *et al*., *Nature* **505**, 195–198 (2014).
7. R. M. Darling, K. G. Gallagher, J. A. Kowalski, S. Ha, F. R. Brushett, *Energy Env. Sci.* **7**, 3459–3477 (2014).
8. G. G. I. Joseph, A. J. Gotcher, G. Sikha, G. J. Wilson, High performance flow battery (2011); www.google.com/patents/US20110244277.
9. J. R. Goldstein, Novel flow battery and usage thereof (2015); www.google.com/patents/US20150048777.
10. "Seventeenth Report of the Joint FAO/WHO Expert Committee on Food Additives. Report No. 539," *Wld Hlth Org. Techn. Rep. Ser.* (World Health Organization, Geneva, 1974).
11. H. Pal, T. Mukherjee, J. P. Mittal, *J. Chem. Soc., Faraday Trans.* **90**, 711–716 (1994).
12. S. Er, C. Suh, M. P. Marshak, A. Aspuru-Guzik, *Chem. Sci.* **6**, 885–893 (2015).
13. M. Quan, D. Sanchez, M. F. Wasylkiw, D. K. Smith, *J. Am. Chem. Soc.* **129**, 12847–12856 (2007).
14. Q. Chen, M. R. Gerhardt, L. Hartle, M. J. Aziz, *J. Electrochem. Soc.* **163**, A5010–A5013 (2015).
15. T. S. Balaban, A. Eichhöfer, M. J. Krische, J.-M. Lehn, *Helv. Chim. Acta* **89**, 333–351 (2006).
16. D. Linden, T. B. Reddy, *Handbook of Batteries* (McGraw-Hill, New York, 2002).

ACKNOWLEDGMENTS

This work was funded by the U.S. Department of Energy Advanced Research Projects Agency–Energy award no. DE-AR0000348 and the Harvard John A. Paulson School of Engineering and Applied Sciences. Methods, along with any additional extended data display items and source data, are available in the supplementary materials; references unique to these sections appear only in the online version of the paper. M.P.M., K.L., R.G.G., and M.J.A. formulated the project. K.L., S.B.K., and D.H. synthesized, analyzed, and purified the compounds. K.L., L.T., and S.B.K. collected and analyzed the NMR and mass spectroscopy data. K.L., A.W.V., and L.E. measured solubility. K.L., Q.C., L.E., and M.R.G. collected and analyzed the electrochemical data. K.L., Q.C., M.R.G., M.P.M., R.G.G., and M.J.A. wrote the paper, and all authors contributed to revising the paper.

SUPPLEMENTARY MATERIALS

www.sciencemag.org/content/349/6255/1529/suppl/DC1
Materials and Methods
Supplementary Text
Fig. S1 to S9
References (*17*–*22*)

7 April 2015; accepted 24 August 2015
10.1126/science.aab3033

H-BONDING CATALYSIS

O–H hydrogen bonding promotes H-atom transfer from α C–H bonds for C-alkylation of alcohols

Jenna L. Jeffrey,* Jack A. Terrett,* David W. C. MacMillan†

The efficiency and selectivity of hydrogen atom transfer from organic molecules are often difficult to control in the presence of multiple potential hydrogen atom donors and acceptors. Here, we describe the mechanistic evaluation of a mode of catalytic activation that accomplishes the highly selective photoredox α-alkylation/lactonization of alcohols with methyl acrylate via a hydrogen atom transfer mechanism. Our studies indicate a particular role of tetra-*n*-butylammonium phosphate in enhancing the selectivity for α C–H bonds in alcohols in the presence of allylic, benzylic, α-C=O, and α-ether C–H bonds.

Complex molecules, such as medicinal agents and natural products, often possess multiple types of C–H bonds, each with a different inherent reactivity. This intrinsic reactivity depends on a multifaceted interplay of steric effects, inductive and conjugative influences, as well as innate strain (*1*, *2*). The intermolecular catalytic functionalization of C(sp^3)–H bonds in a selective manner represents a long-standing challenge that has inspired decades of effort within the synthetic community. Notable early studies by Bergman (*3*), as well as recent advances in selective intermolecular transition metal catalyzed C(sp^3)–H activation—including, among others, Hartwig's rhodium-catalyzed borylation of terminal methyl groups (*4*) and White's iron-catalyzed oxidation of both secondary (2°) and tertiary (3°) aliphatic C–H bonds (*5*)—highlight the importance of catalyst structure on site selectivity.

Catalyst structure has also proven critical to the selectivity of C(sp^3)–H functionalization via hydrogen atom transfer (HAT) catalysis. HAT—the effective movement of a hydrogen atom between two molecular sites—represents a ubiquitous elementary reaction step in organic chemistry (*6*–*8*). The rate of hydrogen abstraction from a C–H bond depends not only on the C–H bond dissociation enthalpy (BDE) but also on polar effects in the transition state. In 1987, Roberts noted that certain electrophilic radicals (such as *t*-butoxyl) preferentially abstract hydrogen from electron-rich C–H bonds, whereas nucleophilic radicals (such as amine-boryl) selectively cleave electron-deficient C–H bonds (*9*). The generality of this concept was subsequently delineated through the broad application of polarity reversal catalysis (PRC), which takes advantage of favorable polar effects to control the regioselectivity of HAT from multiple C–H groups of similar strength (*10*).

We questioned whether the basic principles of PRC could be integrated into a catalytic system for the selective activation of alcohol α-C–H bonds in the presence of a wide range of other C–H bonds (such as α-C=O, α-ether, or allylic or benzylic C–H) (*11*, *12*). Specifically, we postulated that the selective C-alkylation of alcohols could be achieved via a photoredox-catalyzed, H-bond–assisted bond activation strategy (Fig. 1) (*13*–*15*), in which the hydroxyalkyl C–H bond is selectively polarized and weakened via O–H hydrogen bonding.

It is well known that the strength of α C–H bonds of alcohols decreases upon deprotonation of the alcohol O–H group. This so-called "oxy anionic substituent effect" (*16*, *17*) leads to the acceleration of a wide range of organic reactions [such as oxyanionic [1,3] and [3,3] sigmatropic rearrangements and HAT from alkoxides (*18*)]. More recently, it has been shown that intermolecular hydrogen bonding between alcohols and various acceptor molecules gives rise to a similar polarization and weakening of the adjacent C–H bond (*19*), the strength of which is reflected in the ^{13}C nuclear magnetic resonance (NMR) chemical shift and the one-bond ^{13}C–^{1}H coupling constant ($^{1}J_{CH}$) (*20*, *21*). In particular, it was found that a 1 kJ/mol increase in the enthalpy of the H-bond resulted in a 0.2-Hz decrease in $^{1}J_{CH}$ for hexafluoroisopropanol complexed to various amines (*20*). On the basis of these studies, we reasoned that the efficiency and selectivity of alcohol C–H activation

Merck Center for Catalysis, Princeton University, Princeton, NJ 08544, USA.
*These authors contributed equally to this work. **†Corresponding author. E-mail: dmacmill@princeton.edu**

www.sciencemag.org/content/349/6255/1529/suppl/DC1

Supplementary Materials for

Alkaline quinone flow battery

Kaixiang Lin, Qing Chen, Michael R. Gerhardt, Liuchuan Tong, Sang Bok Kim, Louise Eisenach, Alvaro W. Valle, David Hardee, Roy G. Gordon,* Michael J. Aziz,* Michael P. Marshak*

*Corresponding author. E-mail: aziz@seas.harvard.edu (M.J.A.); gordon@chemistry.harvard.edu (R.G.G.); michael.marshak@colorado.edu (M.P.M.)

Published 25 September 2015, *Science* **349**, 6255 (2015)
DOI: 10.1126/science.aab3033

This PDF file includes:

Materials and Methods
Supplementary Text
Figs. S1 to S9

Materials and Methods

Materials

All chemicals were purchased from Sigma Aldrich and used as received unless stated otherwise. 2,6-dihydroxyanthraquinone (2,6-DHAQ) (90% purity) was purchased from AK Scientific Inc. and was recrystallized from DMF-water mixture. 2-methyl-3-hydroxybenzoic acid (98% purity) was purchased from AK Scientific Inc. and was used as received. Nafion 212 and Sigracet SGL 10AA porous carbon paper were purchased from Ion Power and both pretreated (see method below). The cell hardware and Poco pyrosealed graphite flow plates were purchased from Fuel Cell Technologies.

Chemical characterization and preparation

Proton nuclear magnetic resonance (^{1}H NMR) spectra were recorded using Varian INOVA 500 (500 MHz) NMR spectrometers at 23 ℃. Proton chemical shifts are expressed in parts per million (ppm, δ scale) and are referenced to residual protium in the NMR solvent ($CDCl_3$, δ 7.26 ppm; $(CD_3)_2CO$, δ 2.05 ppm; $(CD_3)_2SO$, δ 2.50 ppm; CD_3OD, δ 3.31 ppm). Carbon nuclear magnetic resonance (^{13}C NMR) spectra were recorded using Varian INOVA 500 (125 MHz) NMR spectrometers at 23 ℃. Carbon chemical shifts are expressed in parts per million (ppm, δ scale) and are referenced to the carbon resonances of the NMR solvent ($CDCl_3$, δ 77.16 ppm; $(CD_3)_2CO$, 29.84 ppm; $(CD_3)_2SO$, 39.50 ppm; CD3OD, 49.00 ppm).

Mass spectrum was collected using a maXis impact UHR time-of-flight mass spectrometer system (Bruker Daltonics Inc, Billerica, MA) equipped with an electrospray ionization (ESI) source. The sample was dissolved in acetonitrile (5 uM) and analyzed in negative mode.

2,3,6,7-tetrahydroxyanthraquinone (2,3,6,7-THAQ) was prepared using a previously reported synthetic route *(15)*. The overall yield was 29% (^{1}H and ^{13}C NMR spectra shown in Fig. S8). 1,5-dimethyl-2,6-dihydroxyanthraquinone (1,5-DMAQ) was prepared by the following method: $AlCl_3$ (10 g) and NaCl (1 g) were mixed and heated to 200 ^{o}C to afford a molten salt. 2-methyl-3-hydroxybenzoic acid (2 g) was slowly added in four portions into the $AlCl_3$-NaCl melt. The mixture was continuously heated at 200 ^{o}C for 1 hour. After cool down, distilled water (100 mL) was slowly added to this solution, which was then stirred at room temperature overnight. The dark yellow precipitate was collected on frit glass filter and extracted with ethyl acetate (100 mL). Distilled water (50 mL) was then added to this solution. Ethyl acetate layer was separated from aqueous layer by separatory funnel and dried on magnesium sulfate. The organic phase was concentrated (to approximately 25 mL) and cooled in an ice bath. The resulting precipitates were filtered on celite and washed with cold ethyl acetate (50 mL). This filter cake was then dissolved in acetone (50 mL) where ethyl acetate (50 mL) was added. This mixture was gently heated to remove acetone. Precipitates from this resulting solution were removed on celite. After concentrating the ethyl acetate filtrate, hexane was added to precipitate out desired product which was then collected on frit glass filter and dried under vacuum to afford pale yellow solid. The yield of this product was 12% (^{1}H, ^{13}C NMR spectra and mass spectroscopy results are shown in Fig. S9).

Solubility measurement

Room temperature solubility in 1 M KOH solution was determined by measuring the absorbance at 413 nm and comparing to an absorbance-vs.-concentration calibration curve determined by preparing known concentrations of 2,6-DHAQ. UV-Vis spectrophotometry measurements were performed using an Agilent Cary 60 spectrophotometer equipped with a Quantum Northwest T2 temperature regulator. Appropriate aliquots of 2,6-DHAQ stock solution were added to 1 M KOH blank solution and their UV-Vis absorbance spectra measured. A saturated solution of 2,6-DHAQ in 1 M KOH was prepared by adding 2,6-DHAQ potassium salt into 1 M KOH solution (10 mL) until a thin layer of precipitate formed, the remaining solution was diluted by known proportions, and the absorbance of the resulting solution was compared to the calibration curve.

Electrochemical characterization

A glassy carbon electrode was used for three-electrode cyclic voltammetry tests, except in the electrochemical window tests where graphite foil was used to mimic the condition of porous carbon paper. Rotating-disk electrode (RDE) experiments of 2,6-DHAQ (1 mM) in 1 M KOH solution were performed using a BASi RDE-2 rotating-disk electrode system (Fig. S2A). All tests were carried out using a Gamry Reference 3000 potentiostat, with a Pt counter electrode and a Ag/AgCl reference electrode (equilibrated with 3M NaCl, 213 mV vs. standard hydrogen electrode). A Levich plot was constructed from the RDE data by plotting the mass-transport limited current vs. the square root of the rotation rate (Fig. S2B). The diffusion coefficient of 2,6-DHAQ was calculated for each of three runs from the slope of the line fit to the Levich equation *(17)*. The kinematic viscosity was taken to be 1.08×10^{-6} $m^2 s^{-1}$ *(18)*. The resulting value of the diffusion coefficient is $4.8(2) \times 10^{-6}$ $cm^2 s^{-1}$.

Membrane and electrode pretreatments

Pretreatment of Nafion ® 212 membrane was performed by first heating in 80 ^oC de-ionized water for 20 minutes and then soaking in 5% hydrogen peroxide solution for 35 minutes. These pre-treated membranes were stored in 0.1 M KOH solution at room temperature.

Sigracet ® SGL 10AA (~ 400 μm thickness) porous carbon paper was pretreated by baking in air at 400 ℃ for 24 hours.

Full cell measurement

20 ^oC cycling study

The positive electrolyte was prepared by dissolving potassium ferrocyanide trihydrate (2.56 g) in 1 M KOH solution (15 mL) to afford a 0.4 M ferrocyanide and 2.6 M potassium electrolyte solution. The negative electrolyte was prepared by dissolving 2,6-DHAQ (0.48 g) in 2 M KOH solution (4 mL) resulting a 0.5 M 2,6-DHAQ and 1 M potassium electrolyte solution.

20 ^oC cell performance study

The positive electrolyte was prepared by dissolving potassium ferrocyanide trihydrate (2.56 g) in 1 M KOH solution (15 mL) to afford a 0.4 M ferrocyanide and 2.6 M potassium electrolyte solution. The negative electrolyte was prepared by dissolving

2,6-DHAQ (0.6 g) in 2 M KOH solution (5 mL) resulting a 0.5 M 2,6-DHAQ and 1 M potassium electrolyte solution.

45 °C cell performance study

The positive electrolyte was prepared by heat dissolving potassium ferrocyanide trihydrate (5.1 g) in 1 M KOH solution (15 mL) at 45 °C to afford a 0.8 M ferrocyanide and 4.2 M potassium electrolyte solution. The negative electrolyte was prepared by heat dissolving 2,6-DHAQ (1.2 g) in 3 M KOH solution (5 mL) at 45 °C resulting a 1 M 2,6-DHAQ and 3 M potassium electrolyte solution.

For all full cell studies, the electrolytes were assembled in the fully discharged state.

Cell hardware from Fuel Cell Tech. (Albuquerque, NM) was used to assemble a zero-gap flow cell configuration, similar to previous reports *(19)*. Serpertine flow pattern pyrosealed POCO graphite flow plates were used for both sides. A 5 cm^2 geometric surface area electrode comprised a stack of three sheets of Sigracet SGL 10AA porous carbon paper. A sheet of pretreated Nafion 212 membrane served as the ion-selective membrane. The rest of the space between the plates was gasketed by Teflon sheets. The electrolytes were fed into the cell through PFA tubing, at a rate of 60 mL/min controlled by Cole-Parmer Micropump gear pumps.

Before and during the tests, the electrolytes were purged with ultra-high purity argon to ensure deaeration. Galvanostatic cycling was performed at ± 0.1 A/cm^2, with voltage limits of 0.6 and 1.7 V, controlled by a Gamry 30K Booster potentiostat. To obtain the polarization curves, the cell was first charged to the desired SOC, and then polarized via linear sweep voltammetry at a rate of 100 mV/s. This method was found to yield polarization curves very close to point-by-point galvanostatic holds, yet to impose minimal perturbation to the SOC of the small-electrolyte-volume cell. EIS was performed at 50% SOC, open-circuit potential, and 10 mA/cm^2 AC current density, with frequency ranging from 1 to 100,000 Hz.

Supplementary Text

Cyclic voltammogram modeling

Computation was performed using Mathematica 10.0.1.0 according to algorithms by Oldham and Myland *(20)*. The diffusivity of 2,6-DHAQ and both the one-electron and two-electron reduction products were assumed to be 4.8×10^{-6} cm^2 s^{-1}, based on our RDE studies. The temperature was 293 K. Time was discretized into 40 ms increments, and the current at each time was computed based on the sum of previous currents as described by Oldham *(20)*.

To model the two-electron reduction process (Fig. S2C), the Butler-Volmer equation with the number of electrons n = 2 was used in place of Oldham equation (4:5), and the right-hand-side of equation (8:3) was multiplied by 2 to account for a two-electron reduction *(17, 20)*. The reduction potential was assumed to be equal to the voltage equidistant from the two peaks on the measured cyclic voltammogram (−0.684 V vs SHE) and the charge transfer coefficient α was assumed to be 0.5. The electrochemical rate constant k_0 was then varied from 10^{-3} cm s^{-1} to 10^{-5} cm s^{-1}.

To model the two successive one-electron reductions *(Fig. S2D)*, Oldham equations (12:13) and (12:14) were used *(20)*. The charge transfer coefficients α_1 and α_2 were assumed to be equal to 0.5, and the electrochemical rate constants for the two reductions were assumed equal. The values of the single rate constant and the first and second

reduction potentials were permitted to vary freely. A reasonable fit to the experimental data was observed when the reduction potential of the first reduction $E_1 = -0.657$ V vs SHE, the reduction potential of the second reduction $E_2 = -0.717$ V vs SHE, and the two electrochemical rate constants $k_{0,1}$ and $k_{0,2}$ both equaled 7×10^{-3} cm s^{-1}, a value very close to that observed in other anthraquinone systems *(6)*. The simulation was repeated for $k_{0,1}$ and $k_{0,2}$ equal to 7×10^{-4} cm s^{-1} to establish a lower bound on possible k_0 values.

Energy Density

The negative electrolyte of 0.5 M DHAQ, with two electrons per molecule, has a charge capacity of 27 Ah/L. The positive electrolyte of 0.4 M ferrocyanide has a charge capacity of 11 Ah/L. In the experimental cell used here, in which there is 50% more positive electrolyte than needed to balance the negative electrolyte, the energy density is 6.8 Wh/L. However, eliminating the positive electrolyte volume excess and using established methods of raising the ferrocyanide solubility to 1.4 M *(21)*, the energy density would become 18.8 Wh/L.

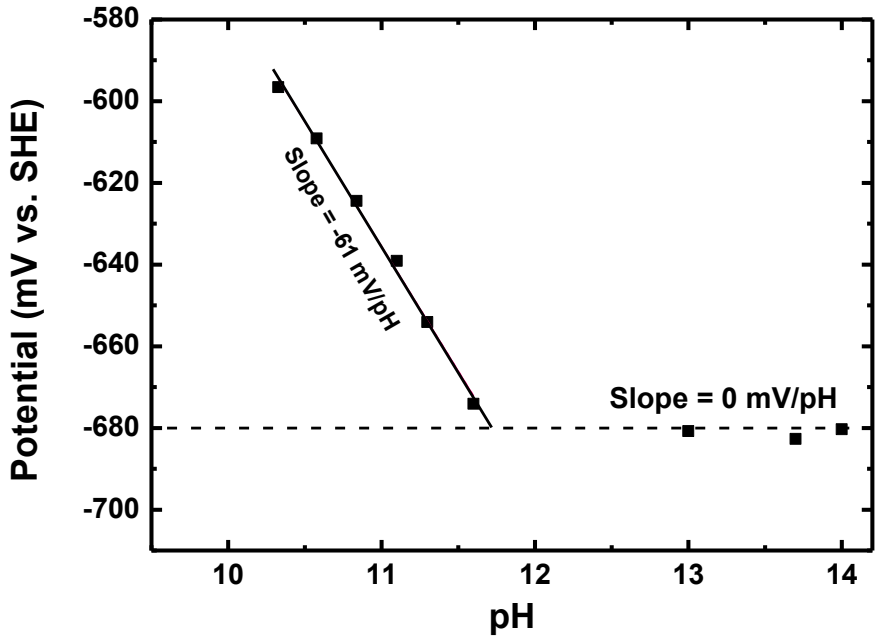

Fig. S1. Pourbaix diagram of 2,6-DHAQ.

Above pH ~11.7, the equilibrium potential of 2,6-DHAQ is pH-independent, indicating that both oxidized and reduced form are fully deprotonated. The solid line is linear fit to the data between pH 10 and 12; the dashed line is not a fit, but zero slope.

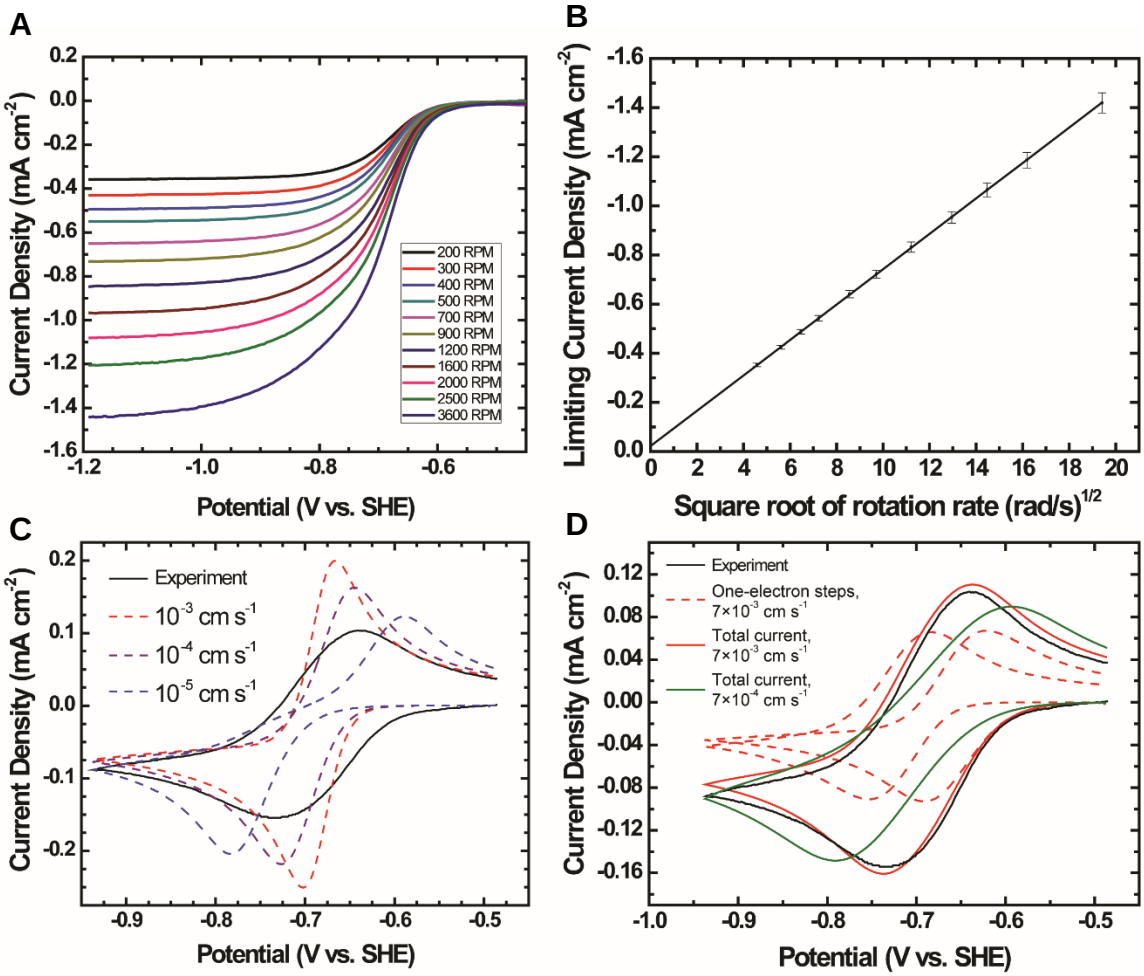

Fig. S2 Study and simulation of the electrochemistry of 2,6-DHAQ.

(**A**) Rotating disk electrode study of the reduction of a 1 mM solution of 2,6-DHAQ in 1 M KOH on a glassy carbon electrode at various rotation rates. (**B**) Levich plot of 1 mM 2,6-DHAQ in 1 M KOH. Data are an average of the current at −1.187 V vs SHE for each of three runs; error bars indicate the standard deviation. (**C**) Cyclic voltammogram of 1 mM 2,6-dihydroxyanthraquinone in 1 M KOH (solid line). Dashed lines represent simulated cyclic voltammograms of a two-electron reduction of varying electrochemical rate constant k_0 and a reduction potential E_0 of −0.684 V vs SHE. The simulations assumed $\alpha = 0.5$. The scan rate in all cases was 25 mV s^{-1}. (**D**) Cyclic voltammogram of 1 mM 2,6-dihydroxyanthraquinone in 1 M KOH (solid black line). Dashed red lines represent the simulated components of two successive one-electron reductions with reduction potentials of −0.657 V vs SHE and −0.717 V vs SHE. The solid red line represents the simulated total current arising from such a reaction. Each simulated reduction has a rate constant $k_0 = 7 \times 10^{-3}$ cm s^{-1}. The same simulation was performed assuming each reduction has a rate constant $k_0 = 7 \times 10^{-4}$ cm, and the total current plotted as a solid green line. The slower rate constants do not adequately describe the observed cyclic voltammogram, setting a lower bound on the value of the rate constant. The simulations assumed $\alpha = 0.5$.

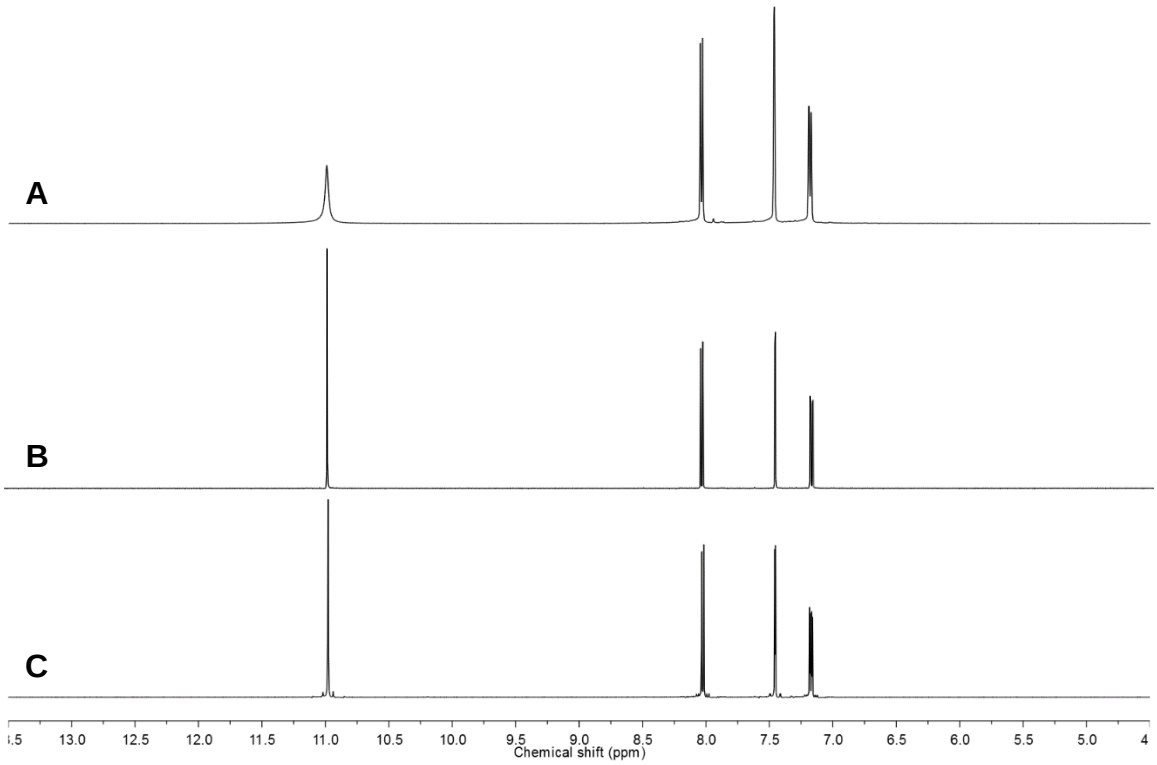

Fig. S3 Chemical and electrochemical stability of 2,6-DHAQ.

^{1}H NMR (500 MHz, DMSO-d_6) spectra. (**A**) 2,6-DHAQ δ: 8.04 (d, 2H, *J* = 8.3 Hz, 2 x ArCH), 7.47 (d, 2H, *J* = 2.5 Hz, 2 x ArCH), 7.19 (dd, 2H, *J* = 8.3, 2.5 Hz, 2 x ArCH). (**B**) 2,6-DHAQ, after 30 days heating in 5 M KOH solution at 100 ºC. (**C**) 2,6-DHAQ, after 100 charge-discharge cycles.

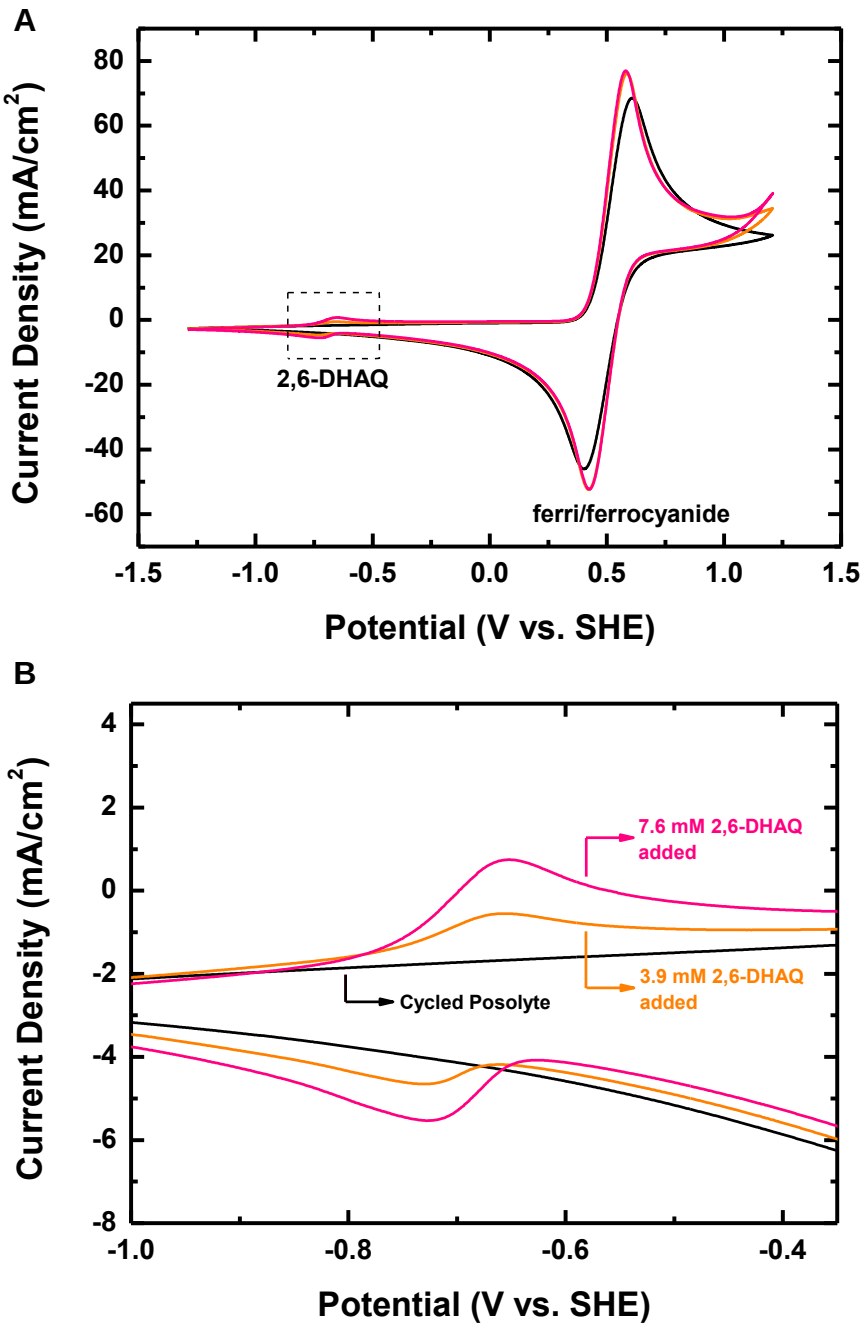

Fig. S4 Test of electrolyte permeation through membrane.

(A) Full and (B) Zoomed in cyclic voltammograms of 0.4 M ferro-ferricyanide electrolyte after 100 charge-discharge cycles (black trace). Same posolyte to which we added 3.9 mM 2,6-DHAQ (orange trace), and 7.6 mM 2,6-DHAQ (pink trace).

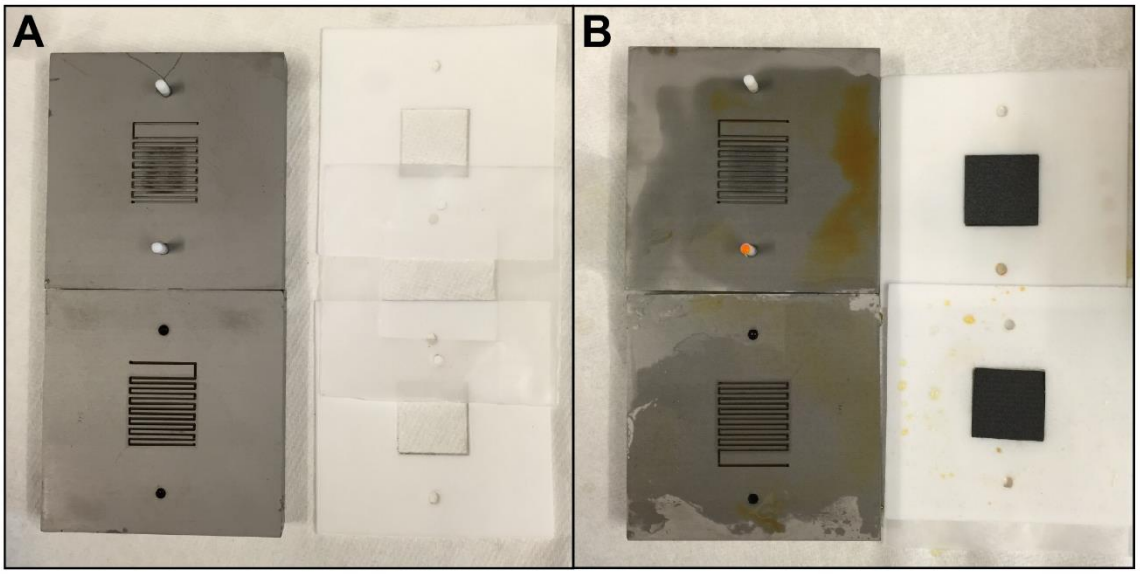

Fig. S5 Leakage of electrolyte into gaskets.

Image showing the Teflon gaskets and graphite flow plates (A) before and (B) after cell cycling. Orange colored area indicates leakage of the negative electrolyte (top plate: negative side; bottom plate: positive side) leading to capacity fade.

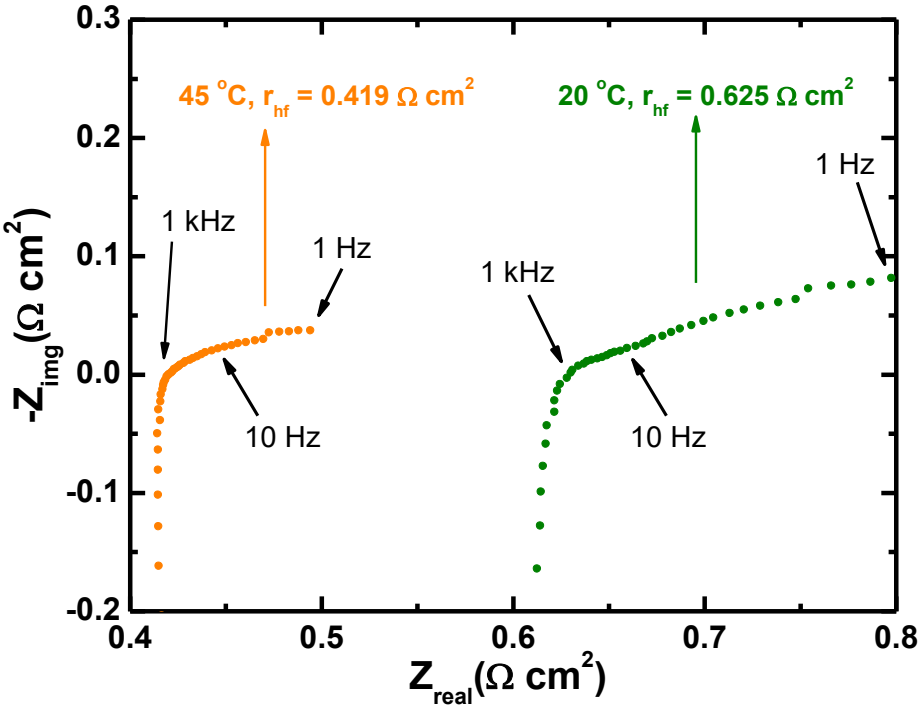

Fig. S6 Electrochemical impedance spectroscopy (Nyquist plot).

Frequency decreases from left to right. The high frequency area-specific resistance (r_{hf}) values discussed in the main text are obtained by fitting the high frequency parts to a resistor (r_{hf}) in series with an inductance component. The inductance came from thick cables and current collectors that connect the cell to the potentiostat. The r_{hf} includes contributions from the Nafion membrane, carbon electrodes, and electrical leads between the cell and the potentiostat. The r_{hf} values at two different temperatures are indicated within the figure.

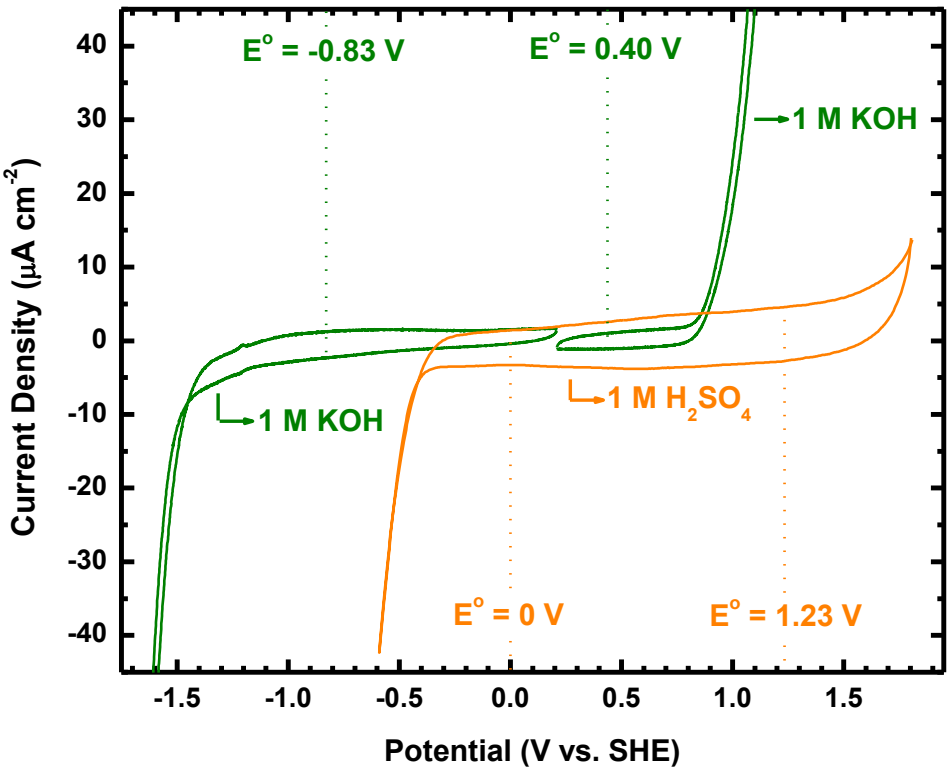

Fig. S7 Background cyclic voltammograms.

Cyclic voltammograms of 1 M KOH and 1 M H_2SO_4 background scanned at 100 mV/s using graphite foil electrode. Dashed lines indicate commonly-reported equilibrium potentials of water splitting reactions. This illustrates the practical stability window for aqueous flow batteries.

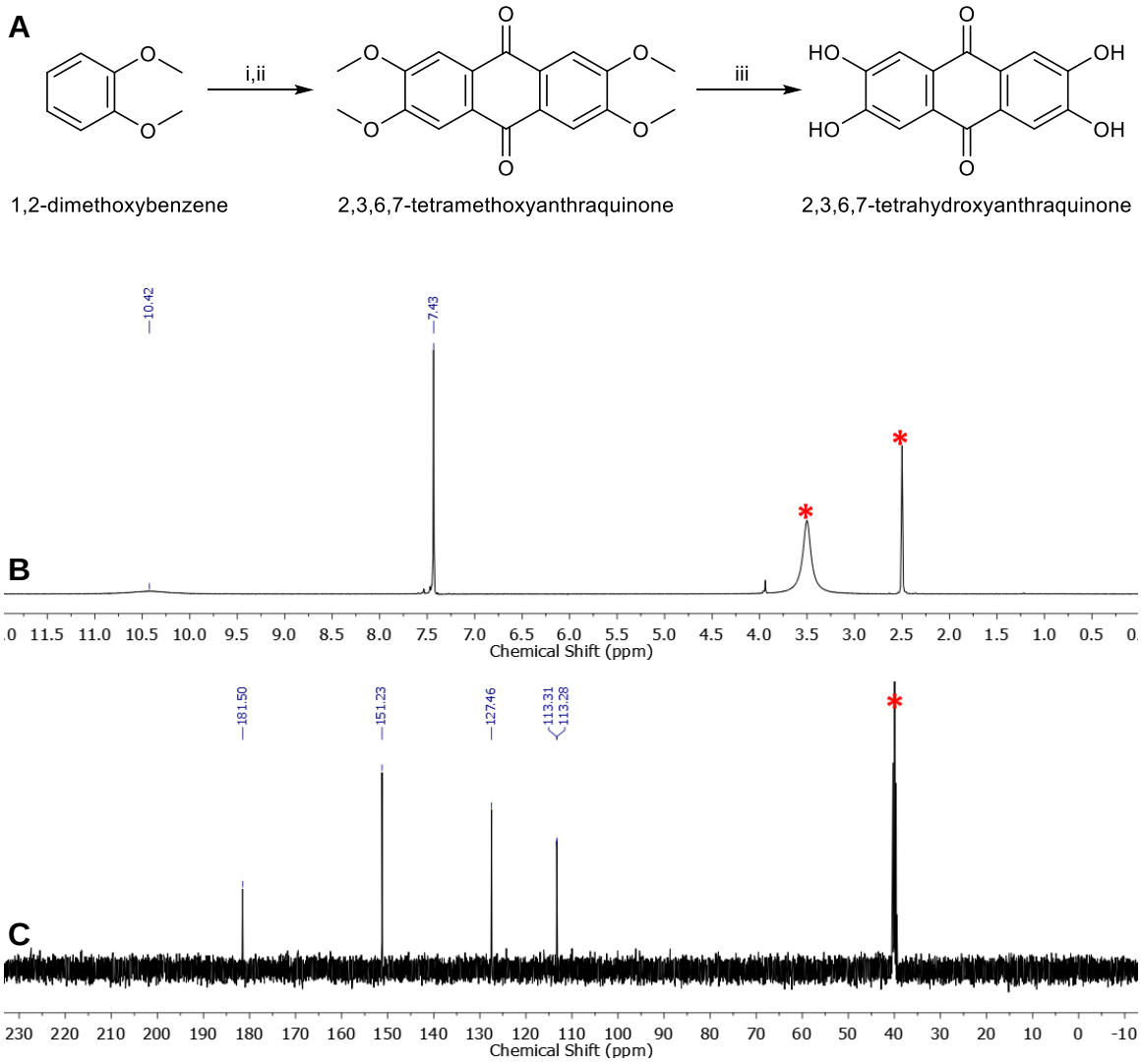

Fig. S8 Synthetic scheme and NMR characterization of 2,3,6,7-tetrahydroxyanthraquinone (2,3,6,7-THAQ).

(**A**) Synthetic scheme of 2,3,6,7-THAQ from inexpensive, commodity chemicals. i. condensation with acetaldehyde to afford 2,3,6,7-tetramethoxydimethylanthracene (MeCHO, H_2SO_4), ii. oxidation to afford 2,3,6,7-tetramethoxyanthraquinone ($Na_2Cr_2O_7$ in acetic acid), iii. hydrolysis of methoxy (HBr, reflux) We carried out all three steps of reaction in this work according to literature reference *(15)*. (**B**) ^{1}HNMR (500 MHz, DMSO) spectrum of 2,3,6,7-THAQ δ 10.42 (br, 4H, 4 x Ar-OH), 7.43 (s, 4H, 4 x ArCH). (**C**) ^{13}CNMR (125 MHz) spectrum δ 181.50, 151.23, 127.46, 113.31, 113.28. Solvent peaks are labeled with asterisks.

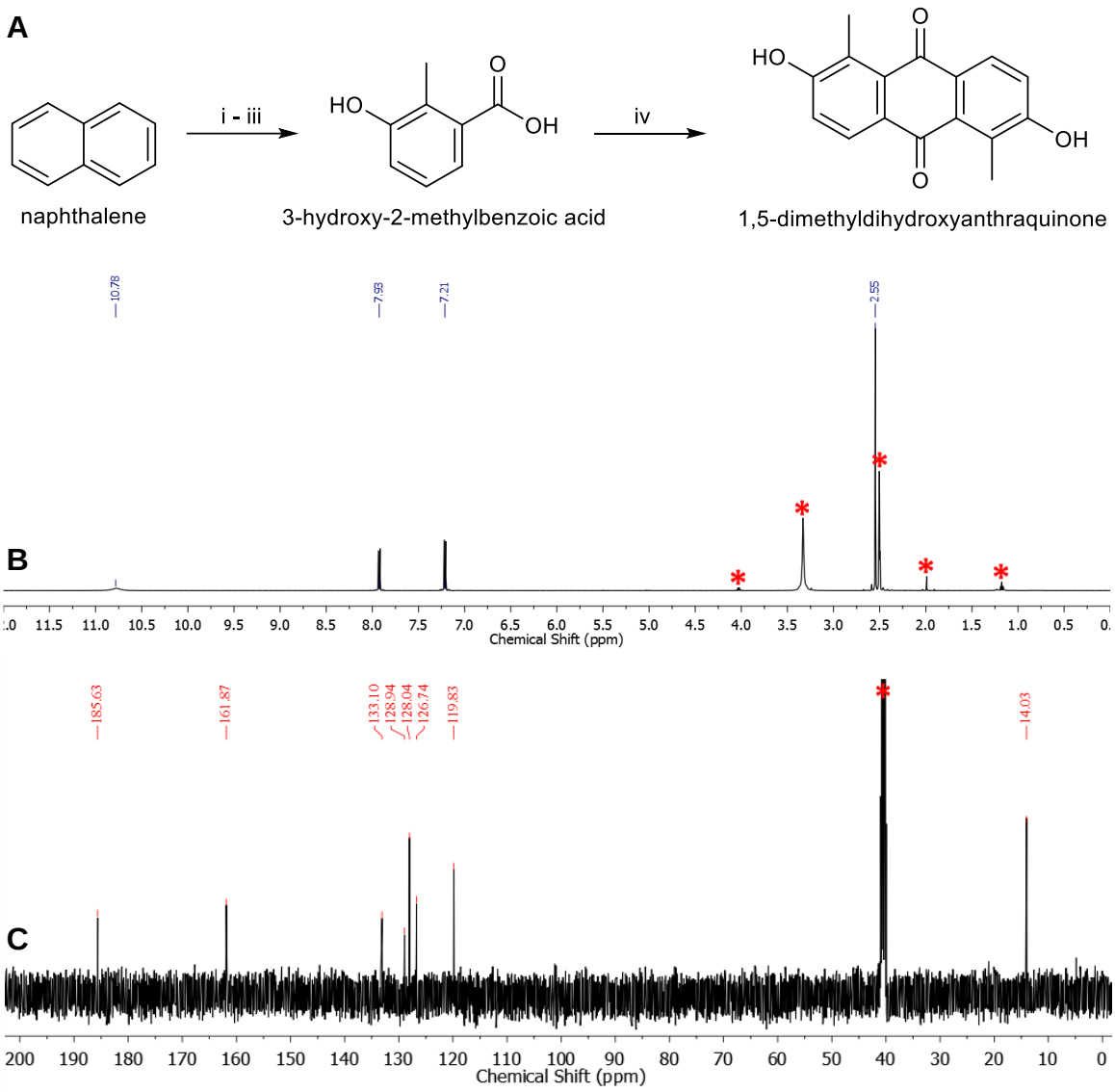

Fig. S9 Synthetic scheme and NMR characterization of 1,5-dimethyl-2,6-dihydroxyanthraquinone (1,5-DMAQ).

(**A**) Synthetic scheme of 1,5-DMAQ from inexpensive, commodity chemicals. i. sulfonation of naphthalene to afford 1,3,5-nanphthalenetrisulfonic acid (H_2SO_4/SO_3), ii. preparation of sodium salt to afford trisodium naphthalene-1,3,5-trisulfonate (NaOH), iii. reaction of trisodium naphthalene-1,3,5-trisulfonate with alkali (NaOH in autoclave at high temperature (280-310 ℃)), iv. Dimerization to afford 1,5-DMAQ ($AlCl_3$-NaCl melt). We carried out step iv in this work. Steps i-iii were reported in a patent application *(22)*. (**B**) ^{1}HNMR (500 MHz, DMSO-d_6) spectra of 1,5-DMAQ δ: 10.78 (br, 2H, 2 x Ar-O**H**), 7.93 (d, 2H, *J* = 8.5 Hz, 2 x ArC**H**), 7.21 (d, 2H, *J* = 8.5 Hz, 2 x ArC**H**), 2.55 (s, 6H, 2 x Ar-C**H**$_3$). (**C**) ^{13}CNMR (125 MHz, DMSO-d_6) δ 185.63, 161.87, 133.10, 128.94, 128.04, 126.74, 119.83, 14.03. Solvent peaks are labeled by asterisk. Mass spectroscopy: C6H12O4 M-H calculated 267.0657 found 267.0659